



<https://doi.org/10.15407/ufm.24.01.038>

M.O. VASYLYEV^{1,*}, B.M. MORDYUK^{1,2,}, and S.M. VOLOSHKO²**

¹ G.V. Kurdyumov Institute for Metal Physics of the N.A.S. of Ukraine,
36 Academician Vernadsky Blvd., UA-03142 Kyiv, Ukraine

² National Technical University of Ukraine
'Igor Sikorsky Kyiv Polytechnic Institute',
37 Peremohy Ave., UA-03056 Kyiv, Ukraine

* vasil@imp.kiev.ua, ** modyuk@imp.kiev.ua

WIRE-FEEDING BASED ADDITIVE MANUFACTURING OF THE Ti-6Al-4V ALLOY. PART II. MECHANICAL PROPERTIES

Currently, the interest in the application of metal additive manufacturing (AM), also known as 3D printing, is grown massively in the various fields of the industry and surgery. AM has significant multiple advantages compared to traditional subtractive technologies for making highly customized parts with complex geometries without causing noteworthy extra costs. Now, several powder-based AM technologies for metals' 3D printing are in progress, in particular, selective laser sintering (SLS), selective laser melting (SLM), and electron-beam melting (EBM). In the past few decades, increasing research and developments are devoted to the wire-feeding-based 3D printing production of parts made of the Ti-6Al-4V alloy, which is widely investigated in different fields such as aerospace, automotive, energy, and marine industries as well as the prosthetics and the production of orthopaedic implants. Due to the feasibility of economical producing large-scale metal components with relatively high deposition rate, low machinery cost, high material efficiency, and shortened lead-time compared to powder-based AM, wire-feeding-based AM (WFAM) is attracting significant attention in the industry and academia owing to its ability for the production of the large components of the medium geometric complexity. In recent years, three options of WFAM are intensively researched, which differ by the wire-melting heating sources: wire + arc additive manufacturing (WAAM); wire-laser AM (WLAM), and wire electron-beam additive manufacturing (WEBAM).

Citation: M.O. Vasylyev, B.M. Mordyuk, and S.M. Voloshko, Wire-Feeding Based Additive Manufacturing of the Ti-6Al-4V Alloy. Part II. Mechanical Properties, *Progress in Physics of Metals*, 24, No. 1: 38–74 (2023)

© Publisher PH "Akadempriodyka" of the NAS of Ukraine, 2023. This is an open access article under the CC BY-ND license (<https://creativecommons.org/licenses/by-nd/4.0/>)

The purpose of the present review is systematic analysis of the mechanical properties of the Ti-6Al-4V alloy samples 3D-printed by WFAM with various heating melting sources, namely, arc, laser, and electron beam. Particularly, considering the literature data for the period of 2013–2020, such important properties as yield strength, tensile strength, elongation, and hardness are analysed for the samples in the as-printed and post-processed conditions.

Keywords: additive manufacturing, 3D printing, Ti-6Al-4V alloy, yield strength, tensile strength, elongation, hardness.

1. Introduction

Additive manufacturing (AM) comprising the three-dimensional printing of solid objects (parts, details) by incremental ‘layer-by-layer’, ‘point-by-point’, or ‘line-by-line’ manner is a group of emerging technologies of highly prospective outcomes considering their versatility, feasibility, obtaining given materials/objects properties, and economical profits. A number of beneficial aspects, as such as in quick and relatively easy producing the goods of high complexity (shape complexity, hierarchical complexity, material complexity, and functional complexity) and a wide variety of 3D printed materials (ceramics, chemicals, composites, concrete, foodstuffs, metals), allow expecting further development and of commercialisation the AM methods [1–4].

It is especially important to use the AM technologies for the production of metallic materials since metals and alloys (including steels, Al-based and Ti-based alloys) are still the main industrial construction materials [4–9]. Additionally, the 3D printed products of complex geometries were shown can be successfully used for many applications in the aerospace, automotive, defence, and medical industries.

Mechanical properties of the 3D printed metallic materials are currently under massive investigation by the scientific community. It is pointed out that a vast majority of the AM produced materials or at least their near-surface layers need to be additionally modified by the post-processing treatments. Heat treatment and/or hot isostatic pressing were reported to provide the improvement of bulk microstructure/properties through structure-phase state transformation and/or residual pores’ healing [10]. Additionally, methods of the surface severe plastic deformation may improve the surface morphology and microstructure in the near-surface layers [10–12]. Both approaches sometime applied in a combined manner can improve key mechanical properties of the 3D printed metallic materials, such as yield strength, tensile strength, hardness, and fatigue life.

Recent studies and practical results have shown that modern AM can eliminate the difficulties in traditional production of such widely used titanium alloy as Ti-6Al-4V. It is known to possess excellent

strength-to-weight ratio, superior biocompatibility, low elastic modulus, and exceptional corrosion resistance. These properties make it attractive for many applications in the aerospace industry, automobile, biomedical, energy, and chemical industries. The optimal strength and ductility of the Ti-6Al-4V alloy products are known can be achieved by appropriate thermal or thermo-mechanical treatment, which determines their microstructure.

The present review analyses the works describing different options of the wire-feeding AM techniques used various wire melting sources (arc, laser, and electron beam), *viz.* wire + arc additive manufacturing (WAAM), wire + laser additive manufacturing (WLAM), and wire electron beam additive manufacturing (WEBAM). A low-cost WEBAM process that exploits standard welding technology has become of interest to the industry. Particularly, this technique allows significantly reducing the product development, and time/labour consuming [13–17].

The main goal of the review is to reveal the features of the obtained mechanical properties of the titanium alloy Ti-6Al-4V 3D printed using the wire feeding AM. In particular, considering the literature data published for the period 2013–2020, such important properties as yield strength, tensile strength, elongation, and hardness are analysed for the samples in the as-printed and post-processed conditions. The analysed works are arranged in chronological order.

2. Wire + Arc Additive Manufacturing (WAAM)

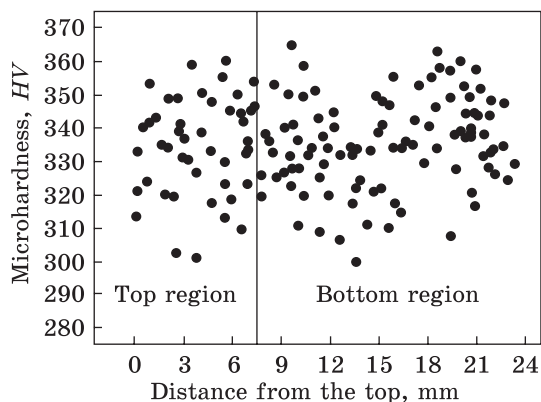
One of the most important tasks in metal 3D printing technology is to achieve uniform mechanical properties along the height of the printed object. In contrast to tensile tests, microhardness measurement makes it possible to solve this problem geometrically more accurately. In this regard, of interest is the work [18] dealing with solving this task using the example of 3D printing by the WAAM. Table 1 shows the main printing parameters.

Received dependency of the microhardness on the distance from the top of the printed sample 07 shown in Fig. 1. According to the authors [18], the microhardness measurements exhibit a certain scatter, which is evidently due to the variation and different orientations of the lamellae within the microstructure. So, no significant difference in hardness is observed between the top region and the banded bottom region. The average hardness is between 311 and 337 *HV*.

The work [19] was performed in order to investigate the influence of the WAAM parameters, location and orientation of WAAM samples on the tensile properties (Table 2).

The tensile A and B specimens have a flat dog-bone shape with a gauge length of 10 mm and the 3×2 mm² cross-section within the gauge

Fig. 1. Dependence of microhardness on the distance from the top of the printed sample 07 [18]



length (for schematic drawings, see Fig. 2). The top-most region of the samples is denoted with location 1. This region has a different microstructure than regions farther down. Locations 2 and 3 refer to the tested region between 1 and 5 cm, and the region more than 8 cm below the top, accordingly. The different H and V orientations characterize specimens with tensile directions horizontal (H) and vertical (V) to the printing plane, accordingly. For tensile tests, the TTDL Instron testing machine at the maximum load of 100 kN was used. The displacement rate was $0.5 \text{ mm} \cdot \text{min}^{-1}$.

Figure 3 demonstrates the ultimate tensile strength and the ductility at room temperature for different orientations and locations, accordingly. As can see, the given values show some distinction for different orientations. So, the ultimate tensile strength (UTS) of the samples with H orientations is slightly higher (983 MPa) than of the samples with V orientation (953 MPa). Whereas UTS not so dependent on the orientation and location, the ductility is more sensitive to these conditions. For example, the ductility is significantly smaller for H -oriented than for V -oriented printed samples and is the smallest (5.1%) for the $H1$ A specimen. For the V -oriented specimens, the spatial dependence of ductility also can be seen. So, the ductility is highest at location 2 (19.1%) in comparison with location 3 (12.5%).

Table 1. WAAM parameters [18]

Specimen number	07
Current during the last depositions, A	180
Table speed, m/min	0.25
WFS of the last deposition, mm/min	1489
Component height, mm	23.5
Wall width near the top, mm	9.8
Number of deposition layers	34
Height of the top region, mm	9.7
Number of parallel bands	22
Band width of the top parallel band, mm	0.65
Ti-6Al-4V wire diameter, mm	1.2
Printing atmosphere	Ar

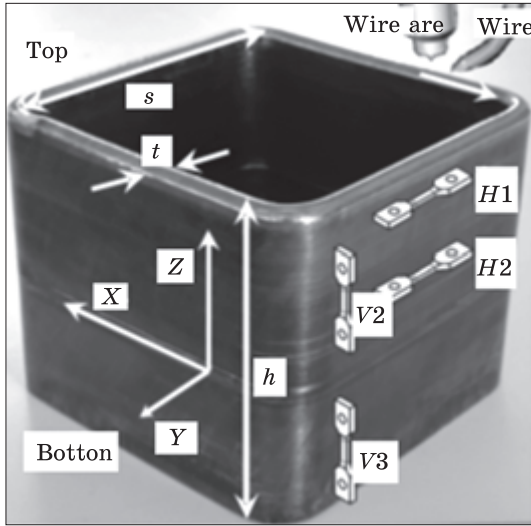


Fig. 2. The as-printed sample scheme: the component with side length s ; the wire arc head; the coordinate system of printing (X , Y , Z directions); wall thickness t and height h ; and the location and orientation of the tensile specimens [19]

The mechanical properties of various regions of the WAAM-printed samples are studied in the paper [20]. The accepted printing parameters, such as arc current, wire feed speed (WFS), and travel speed, as well as the samples and the wire size, are given in Table 3.

For the tensile test, the flat dog-bone shape specimens with a gauge length of 10 mm and a $3 \times 2 \text{ mm}^2$ cross section have been fabricated from different locations and orientations. The following locations within the printed samples have been explored: location 1 refers to the very top region; location 2 comprises the tested region between 1 and 5 cm; location 3 is the region more than 8 cm below the top. For the specimens with horizontal and vertical tensile direction to the deposition plane, the different orientations are labelled as H and V , accordingly. The measured values of UTS and the strain at failure of the above-indicated tensile specimens are shown in Fig. 4. Depending on the orientation and location of the tensile specimens, the UTS is between 929 and 1014 MPa. As can be seen from this figure, the $H1$ location (the top region) of the sample exhibits higher UTS than the $H2$ location (the bottom region).

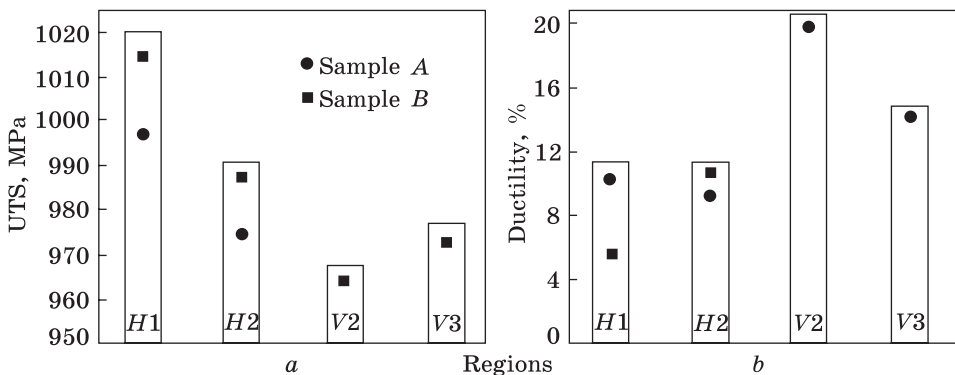
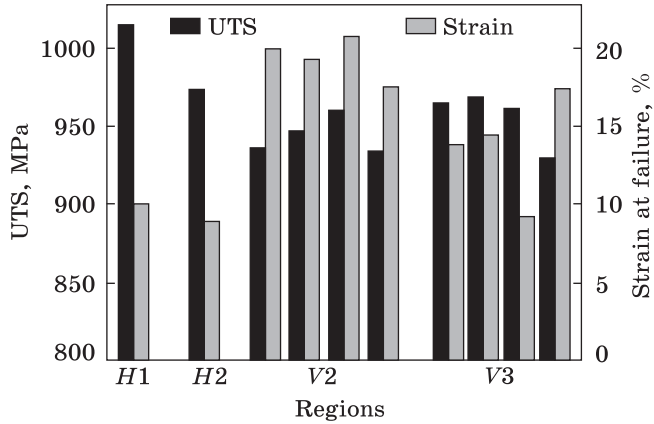


Fig. 3. Ultimate tensile strength (a) and ductility for the printed samples (b) with differences in location and orientation [19]

Fig. 4. UTS and strain at failure of the as-printed samples with different orientations and locations [20]



Also, the UTS for *H* orientations is slightly higher compared with that for *V* orientation and the strain at failure is very sensitive to orientation and lesser to location.

Generally, it is significantly smaller for *H* (9 and 10%) than for *V* orientation (9–21%). Furthermore, the strain at failure is somewhat higher for *V2* than for *V3* tensile direction.

The authors of the study [20] attribute the observed effects of the mechanical properties to the peculiarities of the 3D printed samples grain microstructure. In particular, the differences in the UTS and strain at failure can be related to the α -lath size and the orientation of the elongated, prior β -grains. It is important because of the orientation of these grains, the *H*-oriented tensile specimens contain on average smaller grains and thus a higher amount of grain boundaries than the *V*-oriented specimens do. The grain boundaries are potential sources of failure, and the *H* orientation exhibits a lower strain at failure compared to the *V* orientation.

Table 2. WAAM parameters of the samples *A* and *B* and final geometry [19]

Component name	A	B
Current during the last depositions, A	140	150
Travel speed, m/min	0.25	0.30
Wire feed rate, mm/min	1489	2462
Component height <i>h</i> , mm	24	120
Wall thickness <i>t</i> near the top, mm	9.8	8.8
Number of deposited layers	34	121
Height of the top region, mm	9.7	8.8
Ti-6Al-4V wire diameter, mm	1.2	1.2

Table 3. Deposition parameters (WAAM) [20]

Wire diameter, mm	Wall width, mm	Size, mm	Height, mm	Current, A	WFS, m/min	Travel speed, m/min
1.2	8.8	150	120	150	2.3	0.30

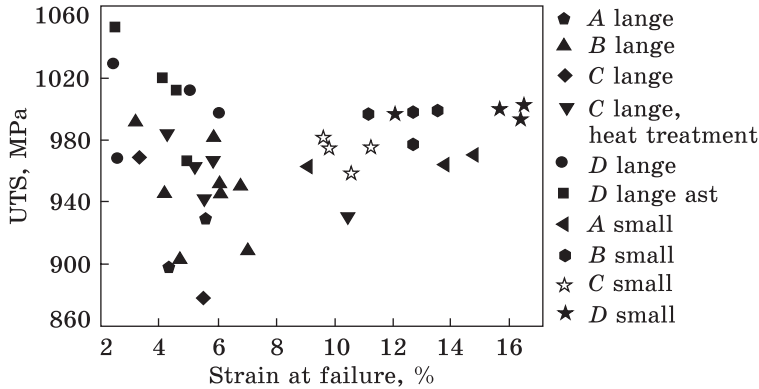


Fig. 5. Summary of UTS and strain at failure of tested samples from components A, B, C, and D, including results from heat treated samples (C) and from tests with higher strain rate (D) [21]

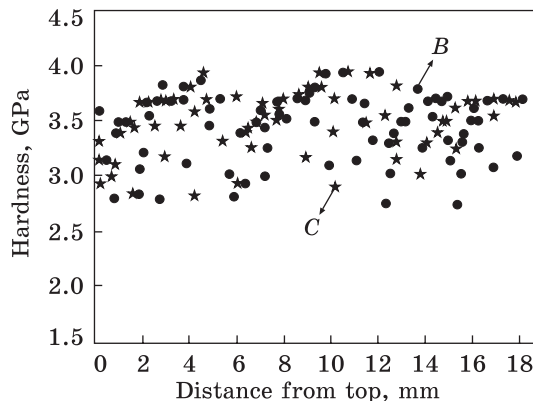
The systematic study of the influence of the printing parameters on the mechanical properties of 3D printed samples was carried out by the authors [21]. Four different samples (A, B, C, and D) were printed using various WAAM parameters and component dimensions that are given in Table 4. The WAAM was performed with the Ti-6Al-4V wire diameter of 1.2 mm.

The tensile samples of larger and smaller types were prepared. The tensile samples of the first type had a gauge length of 35 mm and a cross-section within the gauge length of 4×2 mm², and the samples of the second type had a gauge length of 10 mm and a cross-section within the gauge length of 3×2 mm². The tensile direction of the larger and smaller samples was parallel to the X and Z direction, accordingly. The smaller tensile samples contain the tested region between 2 and 4 cm above the substrate (Ti-6Al-4V). Several of the large samples (component C) were subjected the annealing at 600 °C for 2 h in the vacuum. The measured UTS and strain at failure are summarized for the lar-

Table 4. WAAM parameters, the resulting geometry and mechanical properties of the four printed samples [21]

Printed samples	Deposition parameters			Geometry			Properties	
	Current, A	WFS, m/min	Travel speed, m/min	Height, mm	Wall width, mm	Top region height, mm	Vickers hardness, GPa	Young's modulus, GPa
A	150	2.1	0.30	120	8.8	8.8	3.1	117
B	183	2.2	0.25	70	9.5	8.7	3.2	118
C	163	1.8	0.30	70	8.8	8.2	3.3	121
D	165	1.4	0.25	70	9.5	8.8	3.4	118

Fig. 6. Hardness ($Y-Z$ plane) of printed samples B and C vs. the distance from the top (Z direction) [21]



ge and the small samples in Fig. 5. As can be seen, the UTS varies between 880 and 1054 MPa, and the strain at failure is between 3.0 and 16.4%. Also, the average UTS of samples from component A is the smallest, and

UTS is the highest for component D . There is following output that the small samples exhibit almost a threefold larger strain at failure than the large specimens do. As the authors [21] concluded, the orientation dependence of the strain at failure was attributed to the orientation of the elongated prior β grains, because of providing more grain boundaries. The latest, as it is known, are potential sites of failure, to the tensile specimens oriented in the X -direction (in the present study it is large samples) than to samples in the Z -direction.

According to Ref. [21], the microhardness shows a certain scatter for all components, yet no dependence on the wall height (Fig. 6). Also, the microhardness does not significantly differ in the top and bottom regions of the printed samples (Table 1). In particular, the microhardness increases slightly from 3.1 HV for component A to 3.4 HV for component D . This is consistent with the observations that the UTS is the lowest for component A and the highest for component D . Also, one can see in Table 1 that the measured Young's modulus vary between 117 GPa and 121 GPa, and components A and C respectively exhibit the lowest and the highest values of this characteristic.

In recent years, it has been established that there is anisotropy of the mechanical properties after affecting AM. It is due to the solidification characteristics of Ti-6Al-4V alloy parts microstructure, which is characterised by the strongly textured large columnar prior β grains, parallel to the thermal gradient, hence orientated along the vertical direction. Concerning WAAM, this problem is considered by the authors [22]. The next WAAM parameters were used: wire feed speed $1.6 \text{ m} \cdot \text{min}^{-1}$; travel speed 4.5 mm/s; peak arc current 150 A; pulse duration 0.05 s; frequency 10 Hz. Rolling was used as post-treatment, which was started and finished 35 mm within the deposit, and it was done between passes, with a speed of 3 mm s^{-1} after the material had cooled to room temperature. Three loads were applied: 50 kN and 75 kN. The rolling was used to reduce distortion, because of changes in the geometry of the printed

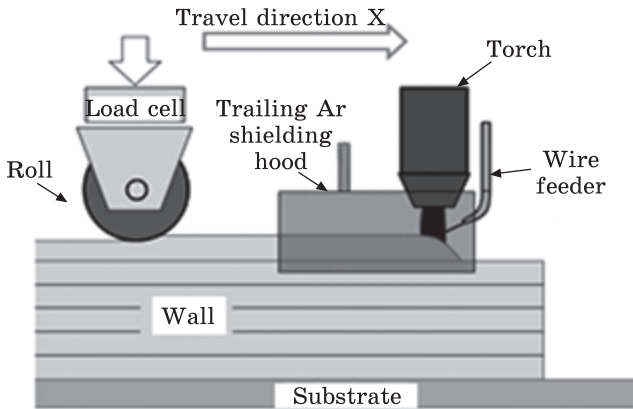


Fig. 7. The schematic view of the combined WAAM rolling process [22]

samples and most likely reduction in residual stress, and reduced variability of the layer height; refine the prior β grains and α lamellae, and change from columnar microstructure to equiaxed one due to recrystallization of the β -phase; improve the mechanical properties; isotropic mechanical properties. The schematic diagram of the combined WAAM rolling process is presented in Fig. 7.

In Figure 8, the tensile test results from the research [22] are compared against the wrought material. It can be seen that for the samples rolled at 75 kN all properties were better than the wrought material and rolling resulted in the improvement of all mechanical properties tested, which were always higher for both horizontal and vertical directions, apart from the elongation of the vertical unrolled specimens. Rolling also affects the hardness. It was found that the hardness values were 374 HV and 377 HV, for the 50 kN and 75 kN samples, respectively and both values are higher than the unrolled sample (367 HV). According to the authors [22], the improvement in the strength and hardness could be due to two reasons: the refinement in the α phase is associated with an improvement of these two mechanical properties; there is a certain amount of cold work during each rolling pass. If speaking about elongation, it must be considered the following factor caused by the refinement of the prior β grains, which has the detrimental effect of this property (so work hardening does). On the contrary, the reduction in α lamellae thickness is beneficial [22], and sometimes one of these factors would prevail over the others. Particularly, in the horizontal direction, elongation firstly decreases (up to 50 kN) and then increases (from 50 kN to 75 kN). Obviously, for the sample loaded with 50 kN, the contribution of the cold work and reduced prior β grain size is more important. However, for the 75 kN loaded sample, the reduction in the α lamellae thickness has the greater effect, given that the elongation increases, even if only slightly. In the case of the vertical direction, the refinement of the prior β grains is the main contribution: the much larger reduction in the grain size is observed along this direction, and elongation always decreases with the load.

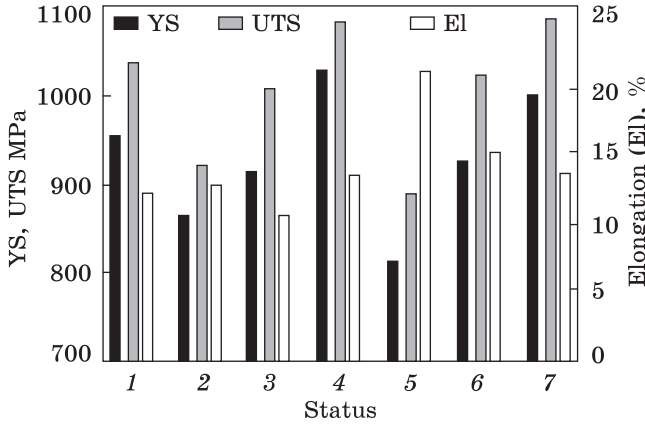
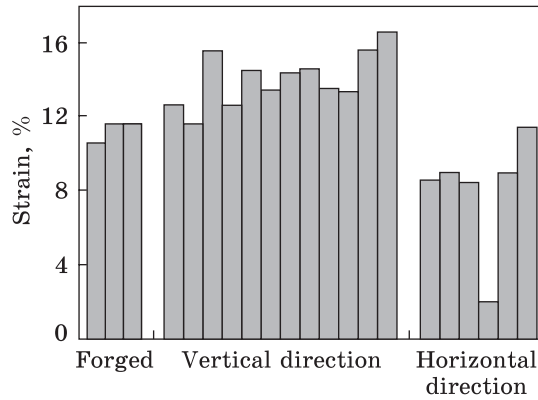


Fig. 8. Comparison of rolled WAAM specimens against unrolled ones: 1 — wrought; 2 — WAAM (horizontal); 3 — WAAM rolled at 50 kN; 4 — WAAM rolled at 75 kN; 5 — WAAM (vertical); 6 — WAAM rolled at 50 kN (vertical); 7 — WAAM rolled at 75, kN (vertical) [22]

Fig. 9. Tensile test results: strain vs samples orientation [23]

The study [23] was devoted to the mechanical properties of the WAAM samples with various orientations using such printing parameters: peak current 180 A; travel speed 0.27 m/min; wire feed speed 1.8 m/min; layer height 1.2 mm; diameter Ti-6Al-4V



wire 1.2 mm. As control samples, the forged Ti-6Al-4V bars, which had the duplex microstructure, were used. The tensile samples were prepared in vertical and horizontal directions. For the tensile tests of the YS and UTS, the Instron 5500R Electromechanical (Instron, Coranation Road, High Wycombe, Bucks) machine with a 100 kN load cell were carried out with the cross-head displacement speed 0.5 mm/min. The tensile samples had a dog-bone shape with a gauge length of 75 mm and a 12.5×2.5 mm cross-section.

As a result of the experiments (Fig. 9), a significant orientation effect on the test samples was found. For the baseline tests, the average YS, UTS, and strain to failure were 950 MPa, 1033 MPa, and 11.7%, respectively. However, the samples of the vertical printing direction exhibited a lower strength, with a mean YS of 803 MPa and UTS of 918 MPa. It can be noted that the tensile strength properties are only moderately anisotropic. Contrary to this fact, the greater asymmetry was observed in the ductility properties, which were much worse when measured in the horizontal direction, transverse to the direction of columnar β grain growth. Evidently, this fact is not that surprising as

when loaded transverse to the prior β grain boundaries, this would be expected to contribute to premature intergranular failure through the grain boundaries.

The following fatigue data were reported in the work [23]: (1) the three baseline samples failed well below 10^6 cycles; (2) sixteen of the as-printed samples did not fail after 10^7 cycles when the test was stopped. In total, twenty one samples had a fatigue life well above three million cycles; (3) because of the limited dataset tested, no statistically valid relationship could be demonstrated between a samples orientation and location; (4) comparing the fatigue test results at this load level, the average high-cycle fatigue resistance of WAAM specimens was shown to be significantly better than that of the forged specimens. This difference can be attributed to intrinsic microstructural differences between the forged and 3D printed alloys.

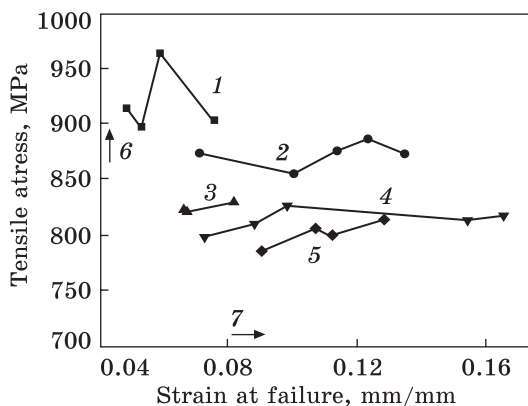
The effects of different post-build treatments on the mechanical properties of the WAAM-produced Ti-6Al-4V components were studied in the work [24]. Experimental Ti-6Al-4V samples were fabricated by WAAM with the Ar trailing shield under the next deposition parameters: arc power 120 A; wire feed 1.5 m/min; wire diameter 1.0 mm. The different post-process conditions of the investigated samples are presented in Table 5.

The mechanical properties of the samples were compared in the as-printing condition, stress-relieved condition, heat-treated condition, and hot isostatic pressing (HIP) condition. The aim of the HIP process including the heat treatment is to close the pores with simultaneously coarsen the microstructure through annealing. It is important to sepa-

Table 5. Summary of the different post process conditions investigated and average mechanical properties for each test condition [24]

Condition	Treatment details	YS (0.2% σ_y), MPa	UTS, MPa	El, %
As-built	Residual stresses are maintained	710	820	7.18
As-built + stress relief	Stress relieved at 753 K or 2 h	766	872	10.9
Hot isostatic pressing	HIP-ed at 1200 K for 2 h dwell @ 1500 Bar argon pressure with 5 K/min heating and cooling rate	712	800	11.0
Vacuum annealing	1200 K for 2 h dwell with 5 K/min heating and cooling rate (same as HIP-ed without pressure)	721	810	11.5
Solution treatment+ aging	Solution treated at 1240 K for 1 h, water quenched then aged at 868 K for 2 h and air cooled	858	918	5.9

Fig. 10. Results of the tensile testing for each test condition: 1 — solution treatment and ageing; 2 — as-printed + stress relief; 3 — as-built; 4 — vacuum annealing; 5 — hot isostatic pressing; 6 and 7 — minimum tensile strength and ductility requirements for Ti-6Al-4V defined in ASTM F1108, respectively [24]



rate the effects of microstructure and porosity on the resulting mechanical properties. Therefore, it was necessary to carry out the additional mechanical test using heat treatment without the porosity elimination process. In this regard, the vacuum heat treatment under identical heating and cooling cycles as that used during the HIP process was performed. During the HIP and the vacuum heat treatments, the microstructure was expected to coarsen and, as the consequence, it may reduce the strength and increase ductility. Accordingly, it was desired to explore the different heat treatments that could preference strength over ductility. One such heat treatment used for Ti-6Al-4V alloy is the solution treatment and ageing (STA), which involves firstly solution treating to develop the larger β -phase fraction followed by quenching and subsequent ageing to decompose the unstable β and promote higher strength.

For tensile tests, the flat dog bone samples ($1.5 \times 5 \text{ mm}^2$ gauge cross-section and 16 mm gauge length) and the Instron machine operated at the crosshead speed of 0.5 mm/min were used. The tensile samples were prepared in the orientations parallel to the 'longitudinal/horizontal build direction' when the tensile axis was normal to the build direction.

The tensile properties for each test condition are presented in Fig. 10 and averaged in Table 5. The authors [24] proposed the following correlation between the features of the phase state and mechanical properties. In particular, there is a correlation between α -plate thickness and colony size, which determines the effective slip length in lamellar microstructures, and therefore, higher strength is achieved under conditions where faster cooling rates take place. The exception to this is the as-built condition (no stress relief) which had a significantly lower tensile strength ($\approx 6\text{--}7\%$) and ductility ($\approx 33\%$) compared with the stress-relieved equivalent, despite both conditions having the same apparent α -phase size and morphology. The residual tensile stresses are known to have a major deleterious effect in this instance. So, the different thermal treatments during WAAM were found to influence directly the

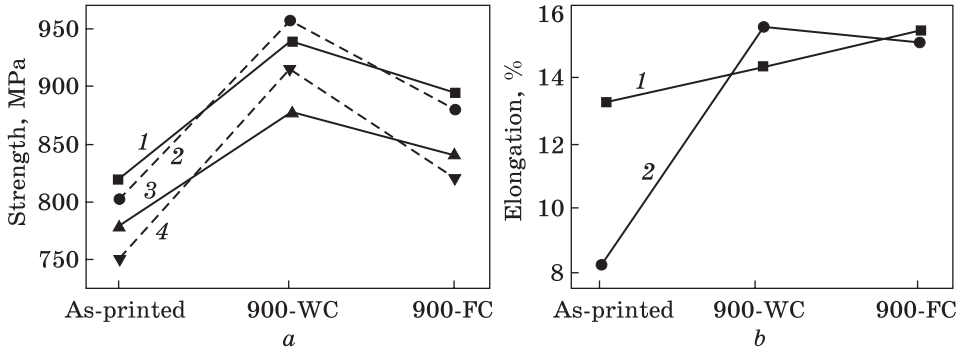


Fig. 11. Tensile properties of the samples; *a* — UTS and YS: 1 — UTS of horizontal sample, 2 — UTS of vertical sample, 3 — YS of horizontal sample, and 4 — YS of vertical sample; *b* — elongation (El): 1 — vertical sample and 2 — horizontal sample [25]

mechanical properties through the well-known Hall–Petch relationship meaning with the α -grain size.

A detailed study of the recrystallization effects during post-heat-treatment of fabricated WAAM samples on mechanical properties was carried out by the authors [25]. The printing in pure argon was carried out by reversed deposition direction with the following parameters: diameter Ti–6Al–4V wire 1.2 mm; arc current of 115 A; wire feed speed of 1.6 m/min; deposition speed of 0.18 m/min; the vertical build interval of 1.1 mm, and the interlayer spacing time of 180 s. The post-heat-treatment was carried out in the furnace with a heating rate of 5 °C/min at the temperature of 900 °C for 2 h with subsequent water-cooling (900-WC samples) and at the temperature of 900 °C for 2 h followed by furnace-cooling (900-FC samples). These post-heat-treatment methods have different recrystallization effects and therefore various influences on the tensile properties of 3D printed samples.

The horizontal and vertical tensile samples were prepared according to standard ASTM E8-04, whose size was 100×10×2 mm³. All tests were carried out at room temperature using the Instron 5500 R with a stress of 6 kN, a frequency of 8 Hz, and a stress ratio of 0.1, and the results are the average of two samples. As the result, the tensile properties of the printed samples were improved owing to the microstructural changes after post-heat-treatment. For example, as one can see from in Fig. 11, *a*, the UTS values of 900-WC and 900-FC samples respectively increase by 117 and 72 MPa in comparison with that of the 3D-printed sample. At the same time, their YS values respectively increase by 110 and 65 MPa. The elongation (El) of the heat-treated sample, especially the horizontal samples, increases. Compared with as-printed samples the El values of the 900-WC and 900-FC horizontal samples are higher by 7.1% and 6.9%. As can be seen in Fig. 14, *b*, it respectively decreases

the ductility anisotropies of the 900-WC and 900-FC samples to 1.2% and 0.2%, as compared to 4.8% in the as-printed sample. The role of grain boundaries (α_{GB}) is also noted. The authors pointed out that the horizontal sample usually exhibited the opening failure mode accelerating the fracture because the continuous α_{GB} is perpendicular to the loading stress. At the same time, the vertical sample is in the sliding failure mode delaying the fracture because the α_{GB} is parallel to the loading stress [26]. For the heat-treated samples, the discontinuous α_{GB} causes the failure mode of the horizontal sample from opening failure to sliding failure, which is the same as that of the vertical sample. This change improves the El of the horizontal sample and reduces the difference in the ductility between two orientations, as well as the ductility anisotropy. Thus, the micro-lamellar recrystallization observed in [25] improves both the microstructure and the tensile properties of the 3D printed titanium alloy.

In recent years, it has been repeatedly proven that the ultrasonic impact treatment (UIT) is an effective technique for surface hardening and residual stress reduction, which is widely used in welding and engineering [10, 12, 27–30]. The most notable effect of the UIT technique is surface nanocrystallization. The authors of the study [31] proposed the novel hybrid process of WAAM and UIT to fabricate 3D printed parts (Table 6).

As shown by the results of mechanical tests, the post-UIT samples have a higher tensile strength than the as-printed samples. For example, the average tensile strength of the post-UIT samples is 934 MPa, while that of the as-printed one is 870 MPa. Microstructural analysis showed that the grain size of the post-UIT samples turned out to be much smaller than that of the as-printed one. This is the main reason for the

Table 6. The process parameters of 3D printing and UIT [31]

WAAM parameters	Values
Type of welding current	Pulsed direct current (DC)
Peak time current	160 A
Pulse frequency	1.6 Hz
Wire feed rate	1 m/min
Scanning speed	120 mm/min
Argon	99.999% purity
Shield gas flow rate	20 L/min
Arc length	5.5 mm
Tungsten electrode diameter	2.4 mm
UIT head scanning speed	50 mm/min
UIT output frequency	20 KHz
UIT output power	0.8 kW

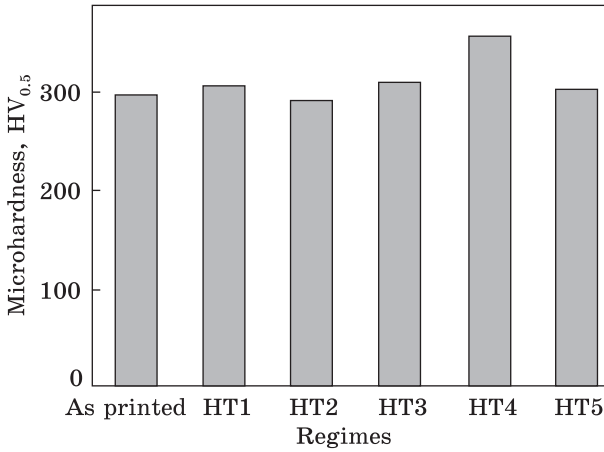


Fig. 12. Microhardness of the as printed and the heat-treated samples [32]

observed improvement in the tensile strength caused because the short columnar and the equiaxed grains replace the coarser columnar grains. No significant difference was observed in the ductility of the post-UIT and as-printed samples. So, the average elongation of both samples is 10.29% and 11.95%, respectively. In addition, the residual stress was significantly reduced after the UIT processes. For example, the single-layer post-UIT samples exhibited a 43% decrease in residual stress compared to the WAAM as-printed samples, while the residual stress reduction was much greater (77.3%) for the seven-layer samples. The authors of the work [31] concluded that the UIT-assisted WAAM could produce 3D printed parts with better performance considering the residual stress, fine microstructure, and mechanical properties. In particular, these results may be helpful in the manufacturing of low-cost and high-wear-resistant titanium alloys.

The importance of the post-heat-treatment to optimize the microstructure of the WAAM parts to satisfy the aeronautical mechanical properties was pointed out in the work [32]. The 3D printing parameters used as follows: the arc current 140 A; the wire feed speed of 2000 mm/min; the scanning speed of 250 mm/min; Ar gas flow rate 20–30 l/min

Table 7. Summary of the heat treatment regimens (AC — air cooling, WQ — water quenching) [32]

Sample types	Heat treatment processes	Application
HT1	600 °C/4 h/AC	Annealing treatment
HT2	850 °C/2 h/AC	—
HT3	930 °C/1 h/AC + 550 °C/4 h/AC	Solution and aging treatment
HT4	930 °C/1 h/WQ + 550 °C/4 h/AC	Solution and aging treatment
HT5	930 °C/1 h/WQ + 800 °C/2 h/AC	Solution and aging treatment

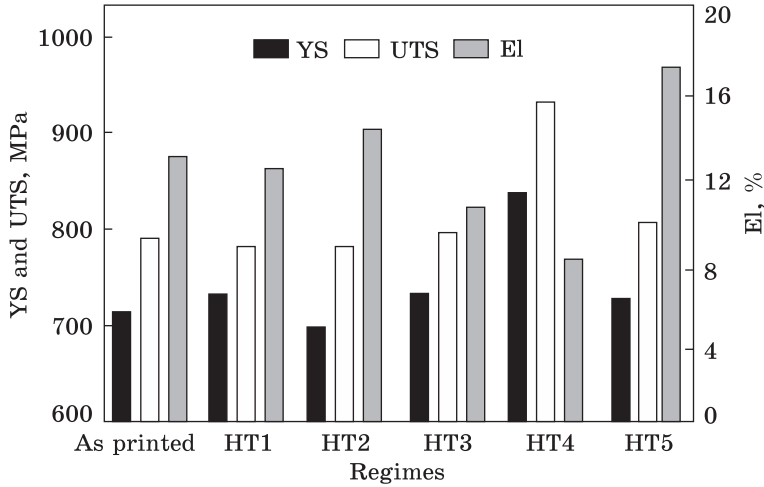


Fig. 13. Tensile properties of the as-deposited and heat-treated samples [32]

into the chamber; Ti-6Al-4V cold wire diameter 1.2 mm. As substrates the hot rolled Ti-6Al-4V plates with dimensions of $200 \times 50 \times 6$ mm³ were used. The types of post-heat-treatment processes are presented in Table 7.

The tensile specimens were made according to ASTM E8 requirements and had a flat dog-bone shape with a 20 mm gauge length, a 6×2 mm² cross-section within the gauge length, and a total length of 50 mm. The uniaxial tensile tests were performed at room temperature using the Instron 3382 testing machine with a crosshead speed of 1 mm/min. The microstructure of the as-printed samples inside the prior- β grains is mainly characterized by continuous prior- β grain boundary α (α_{GB}), Widmanstätten grain boundary α (α_{WGB}), and the intragranular basket weave α .

The microhardness of the as printed and post heat treatment specimens is shown in Fig. 12.

The as-deposited specimen demonstrates an average microhardness of about 298 HV. All tensile properties of the as-printed and post-heat-treated specimens are summarized in Fig. 13. It can see that

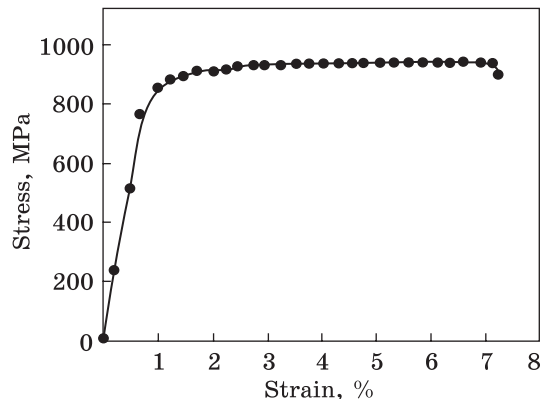


Fig. 14. Representative tensile test with samples extracted in horizontal direction [33]

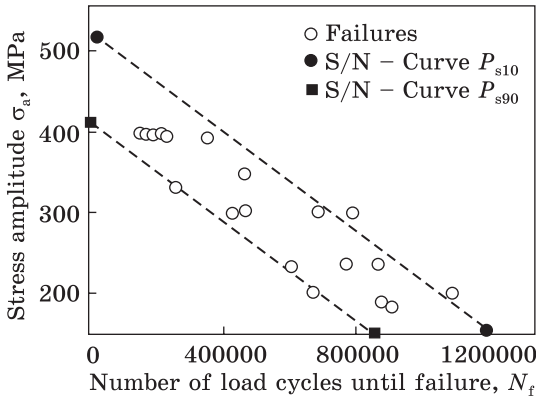


Fig. 15. Results of the fatigue test [33]

the as-printed specimen presents average UTS of about 847 MPa and El of about 12.2%. It is important to note that the highest both the microhardness and the UTS are after HT4 post-treatment, which reach 356 HV and 1034 MPa, accordingly. At the same time, the El is highest for HT5 post-treatment, and the UTS and El are simultaneously increased to 886 MPa, and 16.6%, respectively.

To study the mechanical properties, the authors [33] used the next WAAM parameters: current 92.0 A; voltage 18.1 V; travel speed 2.5 mm/s; wire feed speed 5.0 m/min; wire diameter 1.2 mm. To conduct the quasi-static tensile and fatigue tests, samples were extracted horizontally (parallel) to the printing direction above the sixth layer. This direction was selected to neglect any starting effects related to heating the substrate and, hence, to obtain the comparable microstructure within all samples. To evaluate statistically the mechanical properties and fatigue strength of this AM material, in total 19 fatigue and six tensile samples with a test length of 25 mm were cut out of the three manufactured WAAM parts. The uniaxial, servohydraulic cylinder from Instron Schenck with a maximum load capacity of 25 kN was used in these experiments at room temperature. Mechanical tests were strain-rate controlled until failure of the printed samples and carried out with the touching extensometer and the strain rate of $2.5 \times 10^{-3} \text{ s}^{-1}$. For the fatigue tests the resonant test machine Rumul Microtron with a resonance testing frequency of about 130 Hz. The samples were cyclically tested in the pulsating tension load range with the load stress ratio of $R = 0.1$.

Figure 14 shows the representative stress-strain curve of the horizontally extracted tensile test. One can see that the typical stress-strain curve displays distinctive plastic deformation with a small work-hardening effect. The following summarized mechanical properties of the tensile tests at room temperature extracted in horizontal directions can be noted: mean YS is 867 MPa, mean UTS is 957 MPa, and elongation at the fracture is 6%.

For the fatigue tests, the stress amplitude σ_a was defined using the stress-strain curves. The experimental fatigue test points in the finite life region were evaluated statistically through dint of the standard ASTM E 739 to determine the $S-N$ curves for the survival probabilities

of $P_s = 10\%$ and $P_s = 90\%$. The obtained fatigue test results and the statistically evaluated $S-N$ curves for different survival probabilities are presented in Fig. 15.

3. Wire + Laser Additive Manufacturing (WLAM)

The laser additive manufacturing process (LAMP) which fabricates Ti-6Al-4V alloy is very popular in recent years and has been most widely used to fabricate complex components in sophisticated fields such as aerospace and medical engineering without substantial machining, resulting in less material waste and reduction in lead-time. Direct Laser Deposition (DLD) is the type of LAMP that utilizes metal powder/or wire preforms that are directly deposited to the work site accompanied by simultaneous irradiation of the laser beam. The powder-based selective laser melting (SLM) process was first widely developed and applied in manufacturing [26, 34-36].

Early concepts of the combined energy/material delivery for additive manufacture of metals, including DLD, are rooted in the ‘welding AM’ era as evidenced by the patents of Kratky and Harter [37, 38]. In circa 1980 early concepts of DLD emerged as evidenced by the patent [39] that describes layer-wise, additive deposition via combined laser-powder (or wire) metallurgy. The robotized LAMP system has been developed at University West (Sweden) in close cooperation with Swedish industry [40].

The present review part focuses on laser metal wire printing (LMWP), which is a promising AM technique for larger structures with less complexity. The LMWP process exhibits good material quality with low impurity levels and it also exhibits a relatively high deposition rate, *i.e.*, production speed [41] as compared with powder.

The central part in LMWP is the generation of the beads using a high-power laser source and additive material in the form of metal wire. The laser beam is projected onto the substrate surface and generates the melt pool on the substrate material while the metal wire is fed and melted, forming metallurgical contact with the substrate. By moving the laser processing head and the wire feeder, *i.e.*, the welding tool, relative to the

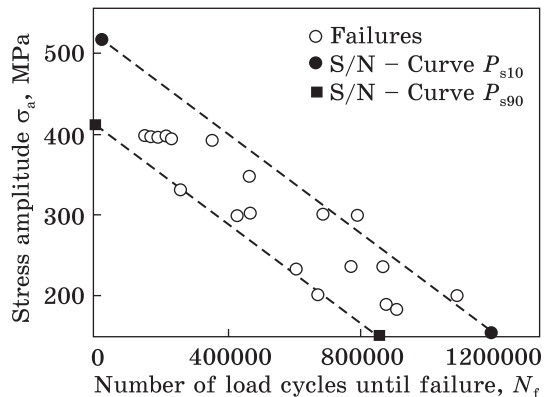


Fig. 16. Schematic view of the wire-feed 3D printing [41]

substrate the part is formed during solidification. The relative motion of the welding tool and the substrate is made using the 6-axis industrial robot arm. The schematic view of such a printing process in the Ar atmosphere is shown in Fig. 16. The main printing parameters are the laser power, the wire feed rate, and the traverse speed. Metal is fed by wire, usually, 1.2 mm in diameter, using the standard wire feeding system. It is important that the wire-based printing processes are sensitive to wire position and orientation relative to the melt pool and the deposition direction. As usually the relatively high-powered laser (e.g., Nd:YAG of wavelength $\lambda = 1064$ nm and with 3.5 kW maximum power) is utilized to create the molten pool.

The main goal of this review part is to get a deeper understanding of the formation of the excellent mechanical properties of the Ti-6Al-4V alloy samples 3D printed by LMWP.

The important mechanical properties including the hardness and the tensile feature of the printed samples using the wire and the high-power diode laser were investigated by the authors [42]. The 1.2 mm Ti-

Table 8. Process parameters for the printing of the single bead walls: 1, 7; 2, 8; 3, 9; 4, 10; 5, 11; 6, 12 — samples for across the building direction. 13, 19; 14, 20; 15, 21; 16, 22; 17, 23; 18, 24 — samples for along the building direction [42]

Sample No.	Laser power, W	Table feed rate, mm/min	Wire feed rate, m/min	Step up, mm
1, 7	2060	100	2	2.5
2, 8	2060	250	2	1.3
3, 9	1650	100	2	2
4, 10	1650	200	2	1.2
5, 11	1200	50	1	2.7
6, 12	1200	150	1	1.2
13, 19	2060	100	2	2.5
14, 20	2060	250	2	1.3
15, 21	1650	100	2	2
16, 22	1650	200	2	1.2
17, 23	1200	50	1	2.7
18, 24	1200	150	1	1.2

Table 9. The Vickers hardness of the samples for different printing parameters [42]

Sample No.	1, 13	2, 14	3, 15	4, 16	5, 17	6, 18
Vickers hardness, $HV_{0.2}$	332	354	340	352	391	339

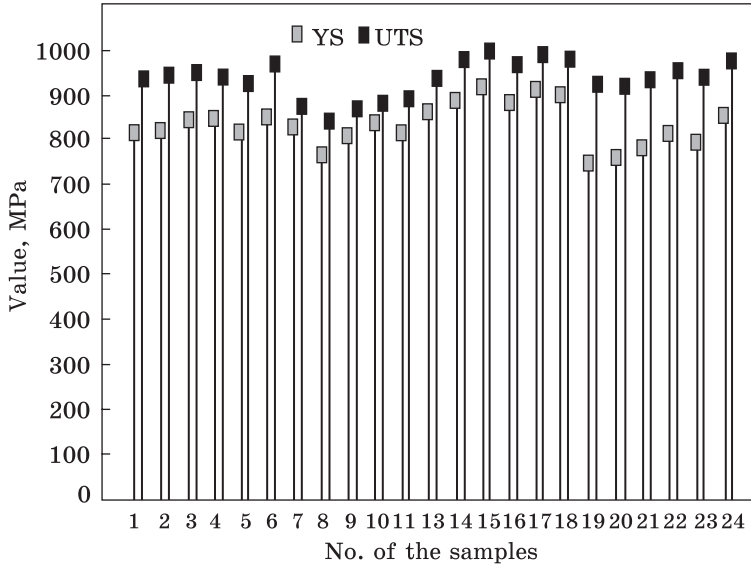


Fig. 17. Comparison of the yield stress and tensile strength for the as-printed and stress relieved samples tested along and across the wall building direction, respectively. Samples 1–11 tested across the building direction; samples 13–24 tested along the building direction; samples 7–11, and 19–24 stress relieved at 700 °C for 2 h [42]

6Al-4V wire was deposited onto the Ti-6Al-4V substrate. The 2.5 kW Rofin DL025 high-power direct diode laser with beam delivery system was utilized in this work. The detailed printing process parameters are shown in Table 8. Selected samples were tested across the building direction and along the building direction. Several samples were post-stress-relieved at 700 °C for 2 h.

Table 9 shows the hardness of the tested samples printed using various different sets of parameters varies less than by 10%. The samples printed with the same laser power at a higher traverse speed possess similar or even slightly higher hardness than the samples printed with a lower traverse speed. Additionally, the laser power increasing enlarges the difference in the hardness. This can be explained by the higher cooling rate during printing with higher traverse speed and/or lower laser power.

The obtained data of the central part of LMWP is the generation of the beads using a high-power laser source and additive material in the form of metal wire. The YS and UTS data obtained for the as printed and the post-stress-relieved samples across the building direction and along the printing direction are shown in Fig. 17, respectively. The higher YS and UTS values were observed in both printing directions. As a result, it was shown that the tensile strength of the as-printed samples is within from 942 MPa to 987 MPa across the printing direction and

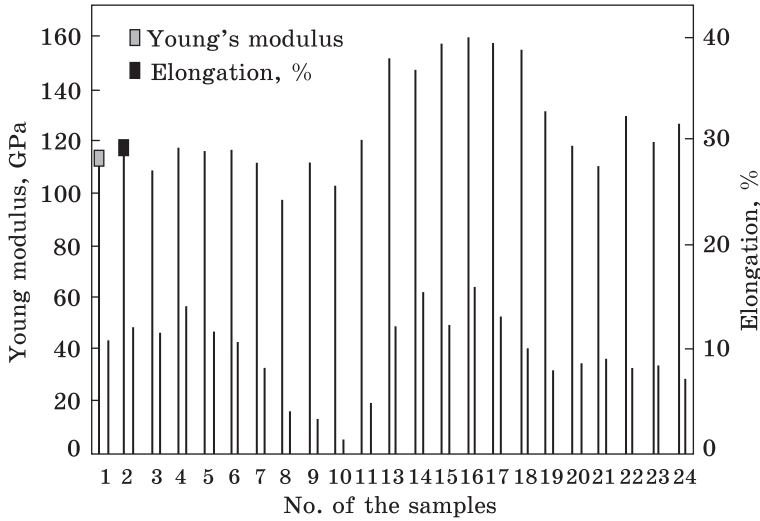


Fig. 18. Comparison of the Young’s modulus and elongation of the as deposited and stress relieved samples tested along and across the wall building direction, respectively. Samples 1–11 tested across the building direction; samples 13–24 tested along the building direction; samples 7–11, and 19–24 stress relieved at 700 °C for 2 h [42]

from 958 MPa to 1011 MPa along the Sample direction, respectively. After post-stress-relieving, the tensile strength for the samples ranges from 864 MPa to 918 MPa across the printing direction and from 937 MPa to 998 MPa along the printing direction, respectively. It is also noted in [42] that the test direction exerts a more significant effect on the YS and UTS than the change in the printing process parameters.

The Young’s modulus (YM) and elongation (EL) of the tested different samples state are shown in Fig. 18. As seen, the YM depends on the printing directions for all the tested samples, and the as-printed samples possess higher YM values than the stress-relieved samples. It is the same trend as YS and UTS, which was discussed above. The as-printed samples have an average YM quantity of 154 GPa, while the stress-relieved ones have average of 123 GPa. Such mechanical parameter of the as-printed samples as El is less sensitive to the test direction. At that time, the El for the stress-relieved samples is dependent on this factor. However, the values are much lower than those of the as-printed samples are. So, the lowest El value from the as-printed samples across the printing direction is about 10.5%, whereas it is less than 2% for the post-stress-relieved one.

The authors [42] noted the important role of the microstructure features on the mechanical characteristics of the printed samples. In particular, in all cases the investigated tensile properties of the samples along the

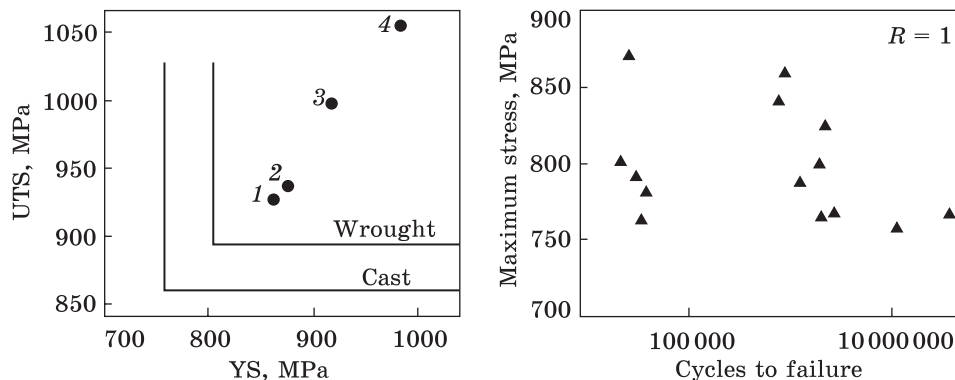


Fig. 19. UTS and YS of as-printed and annealed samples tested parallel (X , Y) and perpendicular (Z) to the printing direction in comparison to the properties of the wrought and the cast alloy: 1 — Z as-printed; 2 — Z , 843 °C/2 h; 3 — X , 843 °C/2 h; 4 — X as-printed [43]

Fig. 20. The high cycle fatigue properties of the samples tested perpendicular to the printing Z -direction after annealing at 843 °C/2 h [43]

printing direction, *i.e.*, parallel to the direction of the β columnar grain growth, are significantly higher than across the grains. It is due to the anisotropic property of the 3D printed materials. Furthermore, both as-printed and post-stress-relieved samples gave similar or even better tensile strength and YM compared with the cast and wrought Ti-6Al-4V alloy.

The authors of [43] fulfilled the experimental investigations including static tensile tests and microhardness measurements of the samples printed by LMWP using the Trumpf HLD 3504 Nd:YAG laser (3.5 kW maximum power), a Weldaix wire feeder, and a Kuka KR100 HA (High Accuracy) 6-axis robot in Ar atmosphere. The tensile samples were extracted from the printed walls at different locations and from different directions. The samples were marked as X if the tensile force was parallel to the printing direction and as Z if one was parallel to the printing direction, *i.e.*, perpendicular to the printed layers. The static tensile tests were performed on a Zwick Z250 at room temperature according to EN 10002 using test velocities of 0.4 mm/min or 1 mm/min, respectively. The samples were tested in the as-printing state and the heat treatment condition (843 °C/2h/furnace cooling). The high cycle fatigue was tested according at room temperature on a Rumul Microtron 654 Resonanz Tester with a test frequency of <120 Hz and the load ratio of $R = 0.1$ at the terminated $4 \cdot 10^7$ cycles.

Figure 19 shows the strength data reserved for the as-printed samples taken from different test directions and some of them after heat-treated conditions. It was concluded that the average data of the YS reach 859–984 MPa, UTS strength 930–1054 MPa. Looking at the average values as the basic data, the heat-treated samples tested in the Z

direction were in the properties range of the wrought material, whereas the annealed printed samples tested in the *X* direction and as-printed samples tested in the *Z* direction are comparable to the cast alloy. The properties of as-printing samples tested in the *X* direction are different from the properties of the cast alloy.

The results of the high-cycle fatigue properties for heat-treated samples in the *Z* direction are presented in Fig. 20. Unfortunately, because of the data scattering the fatigue limit is difficult to define, but it tends to be approximately 700 MPa and it is exceeded the properties of the wrought annealed alloy. The authors [43] pointed out the dependence of mechanical properties on the lamellar microstructure because they are determined by the effective slip length in the α -lamella. The as-printed samples show the very fine lamellar α - β microstructure consisting of the basket weave α (α -lamellae width of $\approx 2 \mu\text{m}$) and few martensitic α grains.

The mechanical tests including the static tension and the high cycle fatigue for the as printed by LMWP, stress-relieved, and annealed conditions were performed in the study [44]. The experimental setup included the Nd:YAG rod laser with a maximum power of 3.5 kW. To prevent oxidation during printing the working chamber was permanently flooded by argon with high purity. The optimal printing parameters are summarized in Table 10.

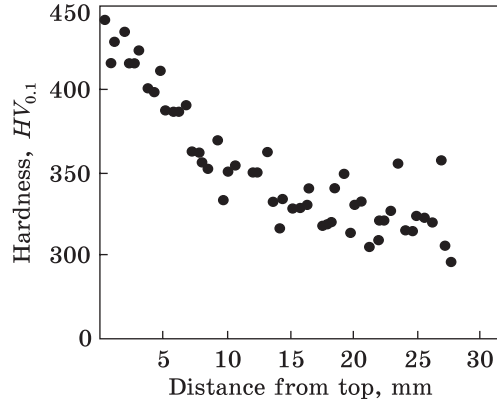
The static tensile tests were performed using the Z250 (Zwick) universal testing machine at room temperature with a test velocity of 0.4 mm/min. The cylindrical, dog-boned specimens had a gauge length of 12 mm and a gauge cross-section of 2 mm. The high-cycle fatigue samples were tested at room temperature on the Microtron 654 (Rumol) resonance tester. The test frequency of ≈ 100 Hz and the load ratio of $R = 0.1$ were used. The test was terminated at $4 \cdot 10^7$ cycles if the sample did not fracture.

Several as-printed samples were also have been subjected to the post-heat treatment. This procedure included the stress relieving treatment at 600 °C for 4 h and annealing at 843 °C for 2 h, both in a vacuum in the range of 10^{-2} to 10^{-5} Pa followed by furnace cooling with roughly 6 °C /min at high temperatures. For mechanical testing, two differently oriented samples were prepared, namely, with a mechanical

Table 10. LMWP process parameters [44]

Parameters	Value	Parameters	Value
Power, kW	3.5	Height increment, mm	1.0
Welding speed, mm/s	10	Deposition rate, kg/h	0.7
Wire-feed speed, mm/s	40	Wall thickness, mm	4–5
Wire diameter, mm	1.2		

Fig. 21. The microhardness vs. the distance from the samples' top region (Y-Z plane) [44]



loading direction parallel to the printing direction (X), and parallel to the direction of the sample height (Z). The Vickers microhardness tests were performed on the cross sections both of the as-printed samples and the heat-treated ones using the load of 100 g ($HV_{0.1}$).

The microhardness $HV_{0.1}$ of the LMWP printed samples in dependence on the location is shown in Fig. 21. As seen, the high microhardness is noted near the top region, and decreasing values towards the constant in the bottom region. The effect of post-heat treatment is presented in Table 11 for the different regions of the printed samples. There is a hardness gradient in the top and the centre area. By all appearances, the different heat treatments do not have an influence on the hardness in the central regions. Possibly, the hardness of the top regions is decreased by the heat treatments.

The results of the tensile tests as the compilation in the form of UTS versus El at failure plots are presented in Fig. 22. It can be concluded that the UTS of the samples prepared in the X direction is larger than that of the samples prepared in the Z direction. Furthermore, the X direction samples show a much smaller El at failure than that registered for the Z direction samples. UTS, it is not easy to observe the reliable effect of heat treatment. However, the El at failure is seen to be increased after the heat treatment at 843 °C. It was concluded that despite the large scatter of the fatigue data the fatigue properties are much better than those required for cast parts and similar or better than those required for wrought parts.

The influence of the LMWP parameters on the mechanical properties of printed samples compared to the plate alloy used in the aerospace specifications was investigated by the authors [41]. Two different sets of printing parameters have been applied and the different sample states were studied: as printed and post-heat-treated. LMWP

Table 11. Microhardness of for different samples state [44]

Samples state	Vickers hardness, $HV_{0.1}$
As-printed	392 ± 14 (top 10 mm) 332 ± 7 (centre 10 mm)
600 °C/4 h	358 ± 16 (top 10 mm) 326 ± 4 (centre 10 mm)
843 °C/2 h	391 ± 11 (top) 330 ± 4 (centre)

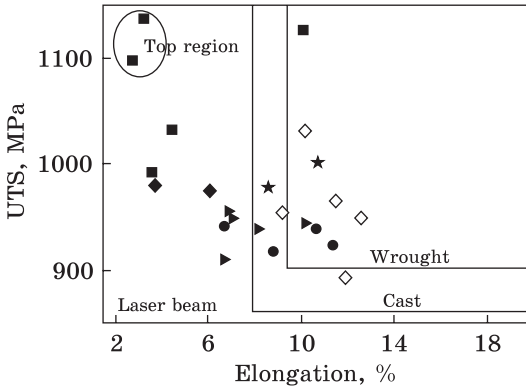


Fig. 22. UTS versus El at failure of the tensile tests [44]

process parameters are shown in Table 12. After final printing, the two post-heat-treatments were performed: stress-relaxation at 600 °C for 4 h followed by furnace cooling to reduce residual stresses without substantial change of the microstructure, β -solution heat treatment at 1200 °C for 2 h followed by furnace cooling,

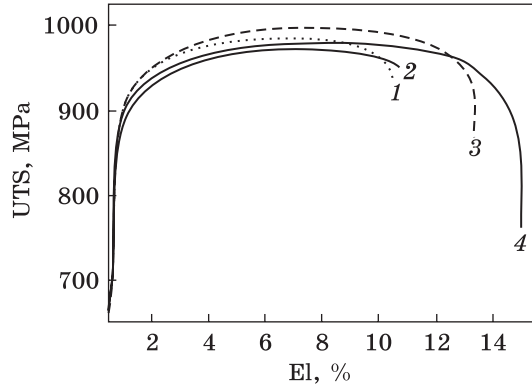
which was performed to investigate the influence of the microstructure on the mechanical properties. The treatment dissolves the columnar prior β -grain morphology and creates equiaxed prior β -grains by furnace cooling. Traditional tensile tests on the samples prepared parallel to the printing direction (*X*-direction) were performed according to European standard EN 10002 at room temperature using the Zwick Z250 machine (displacement controlled at 3 mm/min).

For example, Fig. 23 shows the stress-strain curves for different sets of parameters (P38 and P58). There is a reasonable scatter noticed within the parameter sets. The detailed analysis of the results of the mechanical tests (YS and UTS) allowed the authors [41] to draw the following conclusions. One P38 as-printed sample got the properties of the wrought alloy. One P38 and two P58 as-printed samples achieve at least the properties of the cast material according to the American Society for Testing and Materials. The 600 °C/4 h samples have the highest strength, but also the lowest ductility. The 1200 °C/2 h sample shows the strength below the cast alloy and the ductility compared to the cast alloy. The P58 sample has a higher strength increase than that of the P38 one after the 600 °C/4 h heat treatment. The samples printed at P38 parameters show similar strength properties to those of the material printed with P58 processes. It was also noted that the plate material achieves the strength and ductility of the wrought alloy.

Table 12. LMWP process parameters [41]

Parameter sets	Samples P38	Samples P58
Laser power, kW	3.5	2.625
Deposition or welding speed, mm/s	10	7.5
Wire-feed speed, mm/s	40	30
Diameter of Ti-6Al-4V wire, mm	1.2	1.2
Feeding angle, α	55°	55°

Fig. 23. Stress–strain curves of the as-printed LMWP samples for the different process parameters: 1 and 2 — P58; 3 and 4 — P38 [41]



The most common LMWP systems use a single laser source directed perpendicular to the substrate, and the wire is fed into the melting zone at some angle. The authors [45] investigated the printing ability of the vertical wire feeding with the axisymmetric multi-laser source, and the microstructure and mechanical properties of the printed samples. Such an LMWP system has a strong forming ability with no anisotropic forming problem when fabricating the complex parts in a three-axis machine tool. The schematic image of this printing device with two laser sources is shown in Fig. 24. This device consists of the laser-focusing module, vertical wire feeding module, shielding gas module, and water-cooling module. The WLAM process parameters are given in Table 13.

The mechanical characterization was obtained in the scanning direction (T direction) and printing direction (L direction) of the block samples. The static tensile tests were carried out at room temperature using the Instron 5966 material testing machine. The max load capacity of it is 10 kN and the drive type is powerful motors with a crosshead displacement speed of 0.01 mm/s. The main results of the static tensile tests are shown in Fig. 25. It was noted that the average UTS was 1140.33 MPa with a standard deviation of 11.59 in the T direction and

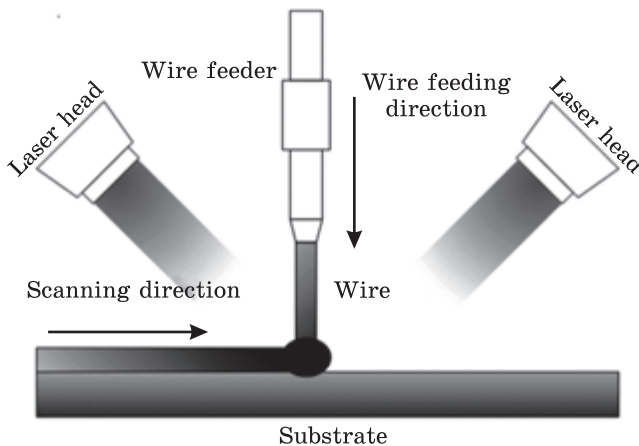


Fig. 24. The schematic of laser additive manufacturing with vertical wire feeding [45]

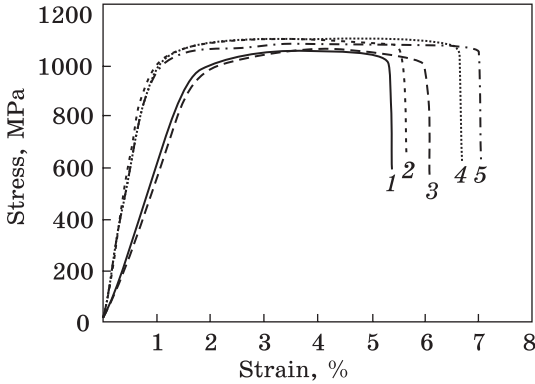


Fig. 25. Ultimate tensile strength and strain of the samples printed by vertical wire feeding with the axisymmetric multi-laser source: 1 — L1; 2 — L2; 3 — T1; 4 — T2; 5 — T3 [45]

Table 13. LMWP parameters used in vertical wire feeding with an axisymmetric multilaser source process [45]

LMWP parameters	Unit	LMWP parameters	Unit
Laser wavelength, μm	976	Wire feed angle, $^\circ$	55
Laser power (total), kW	1.65	Layer thickness, mm	0.8
Diameter of laser beam, mm	3	Diameter of wire, mm	1.2
Deposition speed, mm/min	500	Deposit spacing,	mm
Wire-feed speed, mm/min	2200		

1114.67 MPa with a standard deviation of 20.81 in the *L* direction. However, the increase in the UTS was for the low strain (about 6%). It was also observed that the *T* direction had better strength and ductility than the samples obtained from the *L* direction due to a large number of equiaxed grains. It is important to notice that the vertical wire feeding with an axisymmetric multilaser source at the otherwise process parameters being equal can improve the UTS. Moreover, the anisotropy of the mechanical properties of the printed sample parts can be largely eliminated.

4. Wire + Electron Beam Additive Manufacturing (WEBAM)

A new direction in the development of the AM technology based on using the metal wire as feedstock instead of the metal powder and the electron beam as a heating source was patented in the USA [46, 47]. This new AM technology was named Electron Beam Free Form Fabrication (EBFFF), or later Wire Electron Beam Additive Manufacturing (WEBAM). In this technology, the 3D objects are formed through layered deposition by electron beam melting of the metal wire tip on the metal substrate. The deposition zone (feed point) is moved with a specified speed relative to the substrate resulting in the solidification of the previously deposited material. The feed point is moved sequentially for-

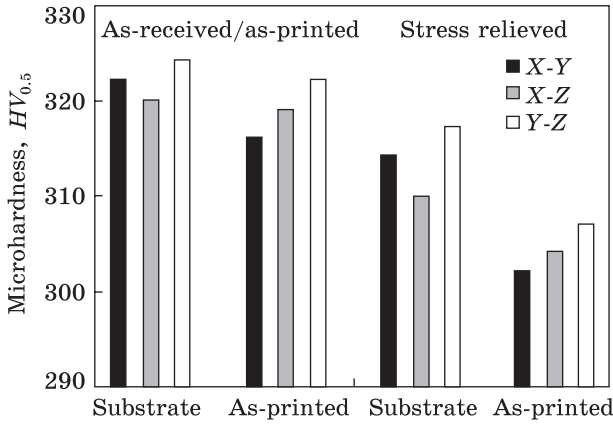


Fig. 26. The average microhardness in the X-Y, X-Z, and Y-Z planes [48]

ming each next layer upon the previous one up to form the complete predetermined 3D part according to the corresponding CAD model. The electron beam falls in WEBAM on the substrate perpendicularly

to its surface and feedstock material is fed to the feed point from aside under some angle. This design uses the electron beam guns of the welding type with a rather high accelerating voltage (60 kV and more). Because of this high voltage, the X-ray radiation from processed parts takes place. As the rule, residual pressure in the operating chamber must be not less than 10^{-1} Pa.

The mechanical properties in the different printing directions were studied by the authors [48]. The accelerating voltage of the electron beam was 60 kV and the wire diameter of 0.9 mm. The WEBAM printing was operated in a vacuum environment with a pressure lower than $6 \cdot 10^{-3}$ Pa. The samples were printed with a wire deposition rate of $25 \text{ mm}^3/\text{s}$ and linear heat input of $90 \text{ J}/\text{mm}$. The substrate and the as-printed tensile samples were cut in the X, Y, and Z directions. These samples were then mechanically tested at room temperature using the 250 kN MTS testing frame integrated with a laser extensometer at the rate of 2 mm/min. The tensile properties evaluated in this work included the YS, UTS, and El for each tensile sample.

The average hardness measured in the X-Y, X-Z, and Y-Z directions of the as-printed samples and the substrate (Ti-6Al-4V) were statistically similar, as can be seen in Fig. 26. The bulk hardness of the as-printed samples $319 \pm 14 \text{ HV}$ was statistically similar to the substrate ($322 \pm 13 \text{ HV}$).

The static tensile properties measured for the Z and X

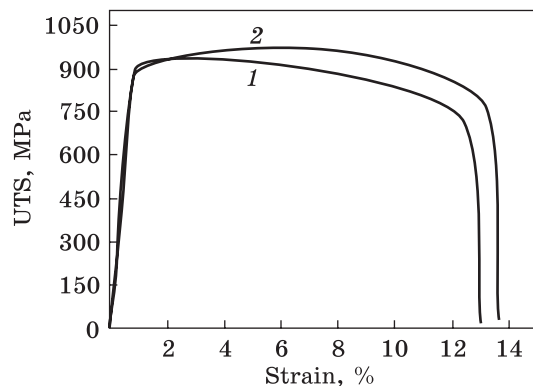


Fig. 27. Typical static tensile behaviour of the as-printed samples: 1 — D_z and 2 — D_x direction [48]

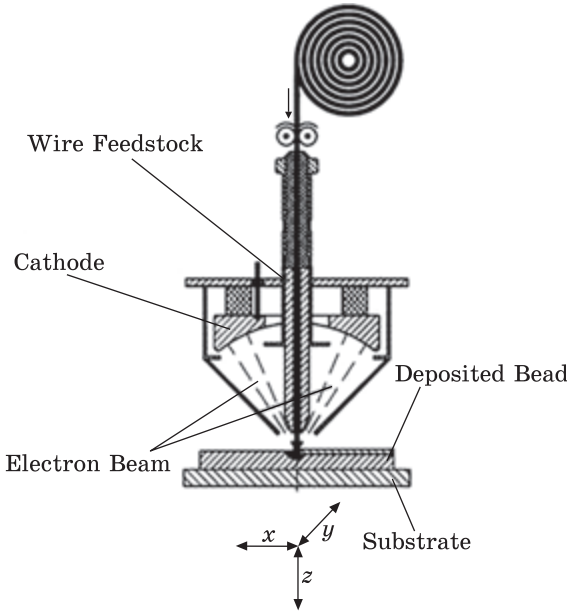


Fig. 28. General design concept of xBeam gun [51]

directions are compared in Fig. 27. As shown, the dependence of the tensile deformation behaviour on the sample orientation was limited and arguably statistically similar in consideration of the standard deviations of these properties. The static tensile properties of the WEBAM Ti6Al4V printed in X and D directions met the minimum requirements of ASTM F2924-14 and ASTM F1108-14 for

the cast Ti-6Al-4V alloy, respectively.

The basic mechanical properties of the Ti-6Al-4V alloy samples (tensile strength, yield strength, elongation, and reduction of area) using the new AM method were determined in the works [49–51]. This

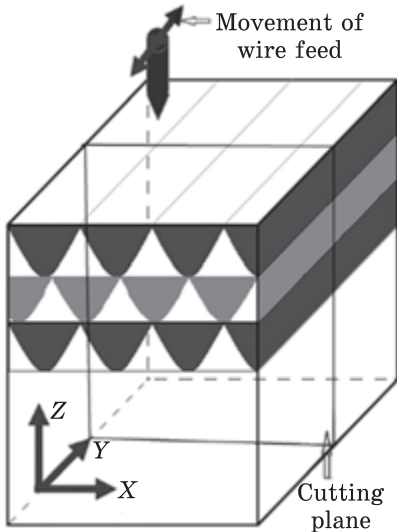


Fig. 29. Scheme illustrating the 'shift strategy' of 3D printing, location of the cut plane for orientations of the mechanical properties of tested samples [50]



Fig. 30. Areas of the printed samples used to the hardness measurements [50]

method, called xBeam, is based on the use of the profile electron beam in the form of a hollow inverted cone to create a melt pool on a substrate and to melt a wire, which is fed coaxially with this electron beam. The general design concept of the xBeam system is shown in Fig. 28. The technical parameters of the 3D printed samples are presented in Table 14. According to a ‘shift strategy’, all beads were deposited in the same direction (along the X co-ordinate), but in each subsequent layer, all beads were deposited with some shift upon the previous correspondent bead along the Y co-ordinate, almost in the middle between the deposition beads of the previous layer (Fig. 29).

The samples for tensile and fatigue testing were cut out from the central areas of 3D printed blocks in three mutually perpendicular directions Z, X, and Y. The tensile testing was performed according to ASTM E8 standard with printed samples having gage diameter and length of 4 mm and 45 mm, accordingly, using Instron 3376 machine with a tension rate was $8 \cdot 10^{-3} \text{ s}^{-1}$. The fatigue tests were carried out for the samples cut from the block printed according to the ‘shift strategy’ using the rotation-bending method at 50 Hz frequency, with a symmetric loading cycle at room temperature with symmetric loading cycle.

The hardness measured in different locations on the sample (Fig. 30) is demonstrated in Table 15. As seen, there is rather negligible difference in the hardness for different cross-section areas for the as-printed samples. Those insignificant differences in hardness for the edges and

Table 14. Characteristics of the xBeam 3D metal printing [49]

Building volume ($W \times D \times H$), mm	300 × 300 × 300
Positioning system	Three-axis, linear
Ultimate power, kW	20
Ultimate accelerating voltage, kV	20
Maximum power consumption, kW	30
Ultimate vacuum, mbar	$5 \cdot 10^{-3}$
Operating vacuum, mbar	$1 \cdot 10^{-2} - 5 \cdot 10^{-1}$
Permissible feedstock type	Wire, rods, cored wire with diameters 1–3 mm
Operating gas (helium) consumption, at 0.1 MPa, l/min	2.5
Recommended installation space (L3W), mm	3300 × 3000 × 2400
Total weight, approximate, kg	1500
Ti-6Al-4V alloy wire diameter	3 mm

Table 15. Hardness of as-printed samples in the different locations [50]

Location (Fig. 7, c)	1	2	3	4	5	6	7	8	9	10	11	12	13
Hardness, HV	328	321	325	329	330	341	335	329	335	334	332	330	329

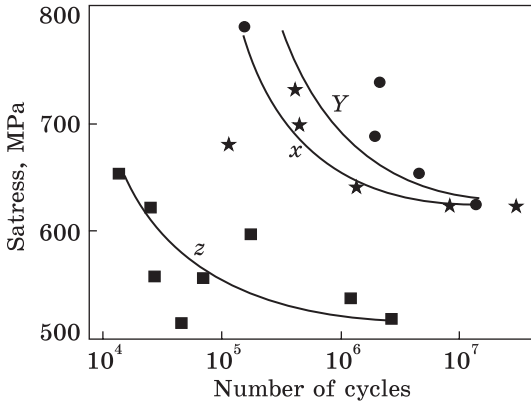


Fig. 31. Fatigue strength data for the printed samples manufactured through the shift strategy in different directions (X, Y, Z) [50]

centre part of the samples because of the repeated heating and cooling of each location during layer-by-layer printing and, hence, the creation of very similar thermal conditions and microstructure for all parts of the block produced.

Results of the tensile tests in different directions are listed in Table 16. From these data, it is clearly observed that characteristics measured for Z direction (across layers lying in the horizontal plane) demonstrate the biggest values scatter. So, the scatter for characteristics of the ductility exceeds half the average value. Both strength characteris-

Table 16. Tensile properties of Ti-6Al-4V material 3D printed with 'shift strategy' [50]

No.	Tested direction	YS, MPa	UTS, MPa	El, %	RA, %
1	Z	972 ± 35	1020 ± 43	8.3 ± 5.4	4.8 ± 3.3
2	Y	975 ± 8	1045 ± 9	9.9 ± 3.6	21.6 ± 7.8
3	X	956 ± 21	1034 ± 22	13.4 ± 5.2	18.7 ± 9.8

Table 17. Mechanical properties of the Ti-6Al-4V alloy samples before and after 3D printing by different wire-feeding based AM

Properties	Wrought	WAAM	WLAM	WEBAM
YS, MPa	760 (ASTM F136)	710 [23] 712 [31]	859-984 [42]	956-975 [50]
UTS, MPa	825 (ASTM F136)	929-1014 [20] 880-1054 [21] 820 [23] 872 [31] 847 [32]	930-1054 [42] 1140 [44]	1020-1034 [50]
El, %	8 (ASTM F136)	12.5-19.1 [20] 7.2 [23] 11.0 [31] 12.2 [32]	6.0 [44]	8.3-13.4 [50]
Hardness, HV	322 (ASTM F136)	311-337 [20] 311-340 [21] 365 [32]	332-339 [42] 332-390 [44]	319 [50]

tics are the highest for the Y direction (along the deposited beads), while elongation and reduction in the area are characterized by the smallest scatter. In general, in this direction, the balance between strength and ductility looks the best and is very close to the level that Ti-6Al-4V alloy has for the cast and wrought state. At the same time, material tested in the X direction (across neighbouring deposited beads) has some intermediate properties for strength and ductility, both in average value and in scatter.

Figure 31 shows the general results of the fatigue tests for the printed samples carved in the Z , Y , and X directions. There are two features related to fatigue test results: (1) the $S-N$ curves reveal the relatively large spread of the fatigue data within each group of the printed samples; (2) it was observed very high fatigue values (maximum value of 770 MPa for the Y direction) and the high fatigue limits similar for the samples in the Y and X direction (about 630 MPa). This fact proves sufficient uniformity of 3D printed alloy and its characteristics for both mutually perpendicular horizontal Y and X directions. In the case of the vertical Z direction, the printed samples are characterized by the lowest fatigue strength with large data scatter. As authors [50–53] suggest, such relatively weaker characteristics are explained by the higher probability of the lack-of-fusion and other manufacturing defects in the samples prepared in the vertical (Z) direction, and the negative influence of noted defects, as well as by the negative influence of essential crystallographic misorientation between parallel printed layers.

Table 17 collects the main mechanical properties obtained by various authors for the Ti-6Al-4V alloy samples 3D printed using different wire-feeding-based AM in comparison with samples produced by standard technique.

5. Conclusions

Nowadays, additive manufacturing (AM) or 3D printing is the new industrial revolution in the world, particularly in various industrial spheres, such as military, aerospace, automobile, and medical, and continues to grow with the addition of new technologies, methods, and applications. At present, materials available for 3D printing include plastic polymers, metals, and biomaterials among many others. One of the most important modern directions of AM is the metal 3D printing. As the analysis of the literature showed that the study of the structure and mechanical properties of samples (parts) α - β titanium alloy (Ti-6Al-4V) obtained using various 3D printing methods is the most important in this regard. This alloy is characterized by an excellent strength-to-weight ratio, superior biocompatibility, low elastic modulus, and exceptional corrosion resistance, and it finds wide applications in the aerospace, automobile, biomedical, energy and chemical industries where

superior specific strength is highly demanded. However, traditional machining is very prolonged and very costly. Recent studies and practical results have shown that modern AM is very competitive compared to conventional manufacturing techniques such as milling, welding, casting, forming, forging, and turning. It is owing to the capability of metal 3D printing to fabricate the three-dimensional metal complex geometries parts, with significant time, cost and waste material reduction.

At present, several different AM technologies for metals 3D printing have been developed, particularly, selective laser sintering (SLS), selective laser melting (SLM), electron beam melting (EBM), and electric arc AM. The main differences between these AMs are the use of different heating sources for selective melting (laser, electron beam, plasma, electric arc) and the feeding materials (metal powder, metal wire, or powder-binder mixture). For the industry manufacturing, technologies with high deposition rates of the economical parts and details of the machines are of the great interest. In this regard, the wire-feeding AM (WFAM) with higher power heat sources is most suitable for such applications. In particular, this AM has been presented to the aerospace manufacturing industry as the unique low-cost solution for producing large thin-walled structures by significantly reducing both product development time and ‘buy-to-fly’ ratios. In recent years, three options of WFAM have been studied, which differ by the wire melting heating sources: wire + arc additive manufacturing (WAAM); wire-laser AM (WLAM), and wire electron beam additive manufacturing (WE-BAM). The purpose of this review was the analysis of the most systematic mechanical properties studies of the Ti–6Al–4V alloy samples 3D printed by WFAM with various heating melting sources, *viz.*, arc, laser, and electron beam.

Numerous studies have established that the structure and, therefore, the mechanical properties of 3D objects significantly depend on the choice of 3D printing parameters. Many publications have found that the macro- and microstructure of the as 3D printed Ti–6Al–4V alloy samples is very different from that of the conventional technologies because of the repeated and rapid thermal cycling that occurs in the layer-by-layer 3D printing process. Such complex thermal cycles lead to the non-uniform distribution of the macro- and microstructure, as well as the mechanical properties of the printed component. To reduce such anisotropy and residual stresses and, therefore, the probability of the cracks’ nucleation, it is necessary after 3D printing to produce the post-processing, particularly, the post-heat-treatment and the post-hot isostatic pressing. In general, the morphology and the size of the columnar prior- β grains and needle-like α -phase lamellae significantly depend on

the WFAM parameters and that determines the desired mechanical properties of the 3D printed parts

Acknowledgements. This work contains results carried out within the projects supported by the National Academy of Sciences of Ukraine (budget program code 6541230) and Ministry of Education and Science of Ukraine ‘Structural-phase control mechanisms of the complex of surface properties of structural and functional alloys by combined thermal, ionic and deformation influences’ (State Reg. No. 0121U109752).

REFERENCES

1. B. Berman, *Business Horizons*, **55**: 155 (2012);
<https://doi.org/10.1016/j.bushor.2011.11.003>
2. D.L. Rakov and R.Y. Sukhorukov, *J. Mach. Manuf. Reliab.*, **50**: 616 (2021);
<https://doi.org/10.3103/S1052618821070116>
3. T.D. Ngo, A. Kashani, G. Imbalzano, K.T.Q. Nguyen, and D. Hui, *Composites Part B: Eng.*, **143**: 172 (2018);
<https://doi.org/10.1016/j.compositesb.2018.02.012>
4. C.W. Hull, *Method and Apparatus for Production of Three-Dimensional Objects by Stereolithography*, Patent US4575330A, Publ. Mar 11, 1986.
5. J.W. Stansbury and M.J. Idacavage, *Dent. Mater.*, **32**: 54 (2016);
<https://doi.org/10.1016/j.dental.2015.09.018>
6. P. Wu, J. Wang, and X. Wang, *Automation in Construction*, **68**: 21 (2016);
<https://doi.org/10.1016/j.autcon.2016.04.005>
7. O. Ivanova, C. Williams, and T. Campbell, *Rapid. Prototyp. J.*, **19**: 353 (2013);
<https://doi.org/10.1108/RPJ-12-2011-0127>
8. M. Vaezi, H. Seitz, and S. Yang, *Int. J. Adv. Manuf. Technol.*, **67**: 1721 (2013);
<https://doi.org/10.1007/s00170-012-4605-2>
9. B. Bhushan, and M. Caspers, *Microsyst. Technol.*, **23**: 1117 (2017);
<https://doi.org/10.1007/s00542-017-3342-8>
10. D.A. Lesyk, S. Martinez, B.N. Mordiyuk, O.O. Pedash, V.V. Dzhemelinskyi, and A. Lamikiz, *Additive Manuf. Let.*, **3**: 100063 (2022);
<https://doi.org/10.1016/j.addlet.2022.100063>
11. E. Atzeni, S. Genna, E. Menna, G. Rubino, A. Salmi, and F. Trovalusci, *Mater.*, **14**: 5366 (2021);
<https://doi.org/10.3390/ma14185366>
12. D.A. Lesyk, S. Martinez, B.N. Mordiyuk, V.V. Dzhemelinskyi, A. Lamikiz, and G.I. Prokopenko, *Surf. Coat. Technol.*, **381**: 125136 (2020);
<https://doi.org/10.1016/j.surfcoat.2019.125136>
13. H.D. Nguyen, A. Pramanik, A.K. Basak, Y. Dong, C. Prakash, S. Debnath, S. Shankar, I.S. Jawahir, S. Dixit, D. Buddhi, *J. Mater. Res. Technol.*, **18**: 4641 (2022);
<https://doi.org/10.1016/10.1016/j.jmrt.2022.04.055>
14. Y.W.D. Tay, B. Panda, S.C. Paul, N.A. Noor Mohamed, M.J. Tan, and K.F. Leong, *Virtual Phys. Prototyping*, **12**: 261 (2017);
<https://doi.org/10.1080/17452759.2017.1326724>
15. L. Mashigo, H. Möller, and C. Gassmann, *J. Southern African Inst. Mining and Metallurgy*, **121**: 325 (2021);
<https://doi.org/10.17159/24119717/1498/2021>

16. S.W. Williams, F. Martina, A.C. Addison, J. Ding, G. Pardal, and P. Colegrove, *Mater. Sci. Technol.*, **32**: 641 (2016);
<https://doi.org/10.1179/1743284715Y.0000000073>
17. D. Ding, Z. Pan, D. Cuiuri, and H. Li, *Robotics and Computer Integrated Manuf.*, **34**: 8 (2015);
<https://doi.org/10.1016/j.rcim.2015.01.003>
18. B. Baufeld, O. van der Biest, and R. Gault, *Int. J. Mat. Res.*, **100**: 11 (2009);
<https://doi.org/10.3139/146.110217>
19. B. Baufeld and O. van der Biest, *Adv. Mater.*, **10**: 015008 (2009);
<https://doi.org/10.1088/1468-6996/10/1/015008>
20. B. Baufeld, O. van der Biest, and R. Gault, *Mater. Des.*, **31**: S106 (2010);
<https://doi.org/10.1016/j.matdes.2009.11.032>
21. B. Baufeld, O. van der Biest, R. Gault, and K. Ridgway, *IOP Conf. Ser.: Mater. Sci. Eng.*, **26**: 012001 (2011);
<https://doi.org/10.1088/1757-899X/26/1/012001>
22. F. Martina, J. Mehnen, S.W. Williams, P. Colegrove, and F. Wang, *J. Mater. Process. Technol.*, **212**: 137 (2012);
<https://doi.org/10.1016/j.jmatprotec.2012.02.002>
23. F. Wang, S. Williams, P. Colegrove, and A.A. Antonysamy, *Metall. Mater. Trans. A*, **44**: 968 (2013);
<https://doi.org/10.1007/s11661-012-1444-6>
24. M.J. Birmingham, L. Nicastro, D. Kent, Y. Chen, and M.S. Dargusch, *J. Alloys Compounds*, **753**: 247 (2018);
<https://doi.org/10.1016/j.jallcom.2018.04.158>
25. Y. Xie, M. Gao, F. Wang, Q. Li, and X.Y. Zeng, *Mater. Sci. Eng. A*, **737**: 310 (2018);
<https://doi.org/10.1016/j.msea.2018.09.076>
26. B.E. Carroll, T.A. Palmer, A.M. Beese., *Acta Mater.*, **87**: 309 (2015);
<https://doi.org/10.1016/j.actamat.2014.12.054>
27. B.N. Mordyuk, G.I. Prokopenko, Y.V. Milman, M.O. Iefimov, and A.V. Sameljuk, *Mater. Sci. Eng. A*, **563**: 138 (2013);
<https://doi.org/10.1016/j.msea.2012.11.061>
28. Y. Kudryavtsev and J. Kleiman, *Weld. Technol.*, **58**: 47 (2014);
<https://doi.org/10.1115/PVP2013-97185>
29. B.N. Mordyuk and G.I. Prokopenko, *Mater. Sci. Eng. A*, **437**: 396 (2006);
<https://doi.org/10.1016/j.msea.2006.07.119>
30. B.N. Mordyuk and G.I. Prokopenko, *J. Sound Vib.*, **308**: 855 (2007);
<https://doi.org/10.1016/j.jsv.2007.03.054>
31. Y.H. Yang, X. Jin, C.M. Liu, M.Z. Xiao, J.P. Lu, H.L. Fan, and S.Y. Ma, *Metals*, **8**: 934 (2018);
<https://doi.org/10.3390/met811093>
32. J. Wang, X. Lin, M. Wang, J.Q. Li, C. Wang, and W.D. Huang, *Mater. Sci. Eng. A*, **776**: 139020 (2020);
<https://doi.org/10.1016/j.msea.2020.139020>
33. S. Springer, M. Leitner, T. Gruber, B. Oberwinkler, M. Lasnik, and F. Grün, *Metals*, **12**: 795 (2022);
<https://doi.org/10.3390/met12050795>
34. Z. Zhao, J. Chen, X.F. Lu, H. Tan, X. Lin, and W.D. Huang, *Mater. Sci. Eng. A*, **691**: 6 (2017);
<https://doi.org/10.1016/j.msea.2017.03.035>
35. M. Thoms, G.J. Baxter, and I. Todd. *Acta Mater.*, **108**: 26 (2016);
<https://doi.org/10.1016/j.actamat.2016.02.025>

36. T. Wang, Y.Y. Zhu, and S.Q. Zhang, *J. Alloys Compounds*, **632**: 513 (2015);
<https://doi.org/10.1016/j.jallcom.2015.01.256>
37. A. Kratky, *Production of Hard Metal Alloys*, Patent US2076952, Publ. Apr. 13, 1937.
38. I. Harter, *Method of Forming Structures Wholly of Fusion Deposited Weld Metal*, Patent US2299747A, Publ. Oct. 27, 1942.
39. C.O. Brown, E.M. Breinan, and B.H. Kear, *Method for Fabricating Articles by Sequential Layer Deposition*, Patent US4323756A, Publ. Apr. 06, 1982.
40. A. Heralić, A.-K. Christiansson, M. Ottosson, and B. Lennartson, *Opt. Laser. Eng.*, **48**: 478 (2010);
<https://doi.org/10.1016/j.optlaseng.2009.08.012>
41. E. Brandl, F. Palm, V. Michailov, B. Viehweger, and C. Leyens, *Mater. Des.*, **32**: 4665 (2011);
<https://doi.org/10.1016/j.phpro.2010.08.087>
42. S.H. Mok, G.J. Bi, J. Folkes, I. Pashby, and J. Segal, *Surf. Coat. Technol.*, **202**: 4613 (2008);
<https://doi.org/10.1016/j.surfcoat.2008.03.028>
43. E. Brandl, C. Leyens, and F. Palm, *IOP Conf. Ser.: Mater. Sci. Eng.*, **26**: 012004 (2011);
<https://doi.org/10.1088/1757-899X/26/1/012004>
44. B. Baufeld, E. Brandl, and O. van der Biest, *J. Mater. Proc. Technol.*, **211**: 1146 (2011);
<https://doi.org/10.1016/j.jmatprotec.2011.01.018>
45. J. Fu, L. Gong, Y. Zhang, Q. Wu, X.Z. Shi, J.C. Chang, and J.P. Lu, *Appl. Sci.*, **7**: 227 (2017);
<https://doi.org/10.3390/app7030227>
46. D.S. Henn, *Solid Freeform Fabrication System and Method*, US Patent 7073561, Publ. Jul. 11, 2006.
47. K.M. Taminger, J.K. Watson, R.A. Hafley, and D.D. Petersen, *Solid Freeform Fabrication Apparatus and Methods*, Patent US7168935 B1, Publ. Jan 30, 2007.
48. P. Wanjara, J. Gholipour, E. Watanabe, K. Watanabe, T. Sugino, P. Patnaik, F. Sikan, and M. Brochu, *Adv. Mater. Sci. Eng.*, **2020**: 1902567 (2020);
<https://doi.org/10.1155/2020/1902567>
49. D. Kovalchuk, O. Ivasishin, and D. Savvakina, *MATEC Web of Conferences*, **321**: 03014 (2020);
<https://doi.org/10.1051/mateconf/202032103014>
50. D. Kovalchuk, V. Melnyk, I. Melnyk, D. Savvakina, O. Dekhtyar, O. Stasiuk, and P. Markovsky, *J. Mater. Eng. Perform.*, **30**: 5307 (2021);
<https://doi.org/10.1007/s11665-021-05770-9>
51. D. Kovalchuk, V. Melnyk, I. Melnyk, and B. Tugaj, *J. Elektrotechnika & Elektronika*, **51**: 37 (2016);
<https://epluse.ceec.bg/wp-content/uploads/2018/08/20160506-full.pdf>
52. O.M. Ivasishin D.V. Kovalchuk, P.E. Markovsky, D.G. Savvakina, O.O. Stasiuk, V.I. Bondarchuk, D.V. Oryshych, S.G. Sedov, and V.A. Golub, *Prog. Phys. Met.*, **24**, No. 1: 75 (2023);
<https://doi.org/10.15407/ufm.24.01.075>
53. M.O. Vasylyev, B.M. Mordyuk, and S.M. Voloshko, *Prog. Phys. Met.*, **24**, No. 1: 5 (2023);
<https://doi.org/10.15407/ufm.24.01.005>

Received 13.10.2022;
in final version, 23.01.2023

М.О. Васильєв¹, В.М. Мордюк^{1,2}, С.М. Волошко²

¹ Інститут металофізики ім. Г.В. Курдюмова НАН України,
бульв. Академіка Вернадського, 36, 03142 Київ, Україна

² Національний технічний університет України
“Київський політехнічний інститут імені Ігоря Сікорського”,
просп. Перемоги, 37, 03056 Київ, Україна

АДИТИВНЕ ВИРОБНИЦТВО СТОПУ Ti-6Al-4V НА ОСНОВІ ПОДАВАННЯ ДРОТУ. ЧАСТИНА II. МЕХАНІЧНІ ВЛАСТИВОСТІ

Наразі інтерес до застосування адитивних методів (AM) для виробництва металів, також відомих як 3D-друк, значно зріс у різних галузях промисловості та хірургії. AM має численні значні переваги порівняно із традиційними технологіями віднімання для виготовлення спеціалізованих деталей зі складною геометрією без значних додаткових витрат. В даний час розробляються декілька порошкових AM-технологій для 3D-друку металів, зокрема селективне лазерне спікання (SLS), селективне лазерне топлення (SLM) і топлення електронним променем (EBM). В останні кілька десятиліть все більше досліджень і розробок присвячено виробництву 3D-друком деталей зі стопу Ti-6Al-4V на основі подачі дроту, який широко досліджувався в різних галузях, таких як аерокосмічна, автомобільна, енергетична та морська промисловість, а також протезування та виробництво ортопедичних імплантатів. Завдяки доцільності економічного виробництва великомасштабних металевих компонентів із відносно високою швидкістю осадження, низькою вартістю обладнання, високою ефективністю матеріалів і скороченим часом виготовлення порівняно з порошковими AM саме AM на основі подачі дроту (WFAM) привертає значну увагу у промисловості та наукових колах завдяки своїй здатності виробляти великі компоненти середньої геометричної складності. В останні роки інтенсивно досліджуються три варіанти WFAM, які відрізняються джерелами нагрівання та топлення дроту: топлення дугою — wire + arc additive manufacturing (WAAM); топлення лазером — wire-laser AM (WLAM); топлення електронним променем — wire electron-beam additive manufacturing (WEBAM). Метою даного огляду є систематичний аналіз механічних властивостей зразків стопу Ti-6Al-4V, 3D-друкованих за допомогою різних нагрівальних джерел топлення дроту (WFAM), а саме, дуги, лазера та електронного променя. Зокрема, розглядаючи літературні дані за період 2013–2020 рр., аналізуються такі важливі для практики властивості зразків у стані після друку та після оброблення, як межа плинності, міцність на розрив, видовження та твердість.

Ключові слова: адитивне виробництво, 3D-друк, стоп Ti-6Al-4V, межа плинності, міцність на розрив, видовження, твердість.